Numerical linearized MHD model of flapping oscillations

D. B. Korovinskiy’ , I. B. Ivanov, V. S. Semenov, N. V. Erkaev, and S. A. Kiehas

Citation: Physics of Plasmas **23**, 062905 (2016); doi: 10.1063/1.4954388
View online: http://dx.doi.org/10.1063/1.4954388
View Table of Contents: http://aip.scitation.org/toc/php/23/6
Published by the American Institute of Physics

PHYSICS OF PLASMAS **23**, 062905 (2016)

Numerical linearized MHD model of flapping oscillations

D. B. Korovinskiy,[1,a)] I. B. Ivanov,[2,3] V. S. Semenov,[2] N. V. Erkaev,[4,5] and S. A. Kiehas[1]
[1]*Space Research Institute, Austrian Academy of Sciences, 8042 Schmiedlstrasse 6, Graz, Austria*
[2]*Saint Petersburg State University, 198504 Ulyanovskaya 1, Petrodvoretz, Russia*
[3]*Theoretical Physics Division, Petersburg Nuclear Physics Institute, 188300 Gatchina, Russia*
[4]*Institute of Computational Modelling, Russian Academy of Sciences, Siberian Branch, 660036 Krasnoyarsk, Russia*
[5]*Siberian Federal University, 660041 Krasnoyarsk, Russia*

(Received 27 April 2016; accepted 9 June 2016; published online 27 June 2016)

Kink-like magnetotail flapping oscillations in a Harris-like current sheet with earthward growing normal magnetic field component B_z are studied by means of time-dependent 2D linearized MHD numerical simulations. The dispersion relation and two-dimensional eigenfunctions are obtained. The results are compared with analytical estimates of the double-gradient model, which are found to be reliable for configurations with small B_z up to values ~ 0.05 of the lobe magnetic field. Coupled with previous results, present simulations confirm that the earthward/tailward growth direction of the B_z component acts as a switch between stable/unstable regimes of the flapping mode, while the mode dispersion curve is the same in both cases. It is confirmed that flapping oscillations may be triggered by a simple Gaussian initial perturbation of the V_z velocity.
[http://dx.doi.org/10.1063/1.4954388]

I. INTRODUCTION

We present a numerical study of kink-like flapping oscillations performed by means of time-dependent two-dimensional linearized magnetohydrodynamic (MHD) simulations. Flapping oscillations are long-wavelength perturbations propagating in the magnetotail current sheet in transversal direction, mainly from the central part of the sheet towards the flanks, registered in the Earth, Venus, Jupiter, and Saturn magnetospheres.[1–17] Typically (for Earth magnetotail conditions), flapping waves are observed in the central part of the midtail at distances of $10-30\,Re$, where Re is the Earth radius, propagating with a speed of $20-60\,\mathrm{km/s}$ ($\sim$10 times less than the Alfvén velocity), an amplitude of $1-2\,Re$, and a quasiperiod of several minutes. Flapping motions in the distant magnetotail are reported in Refs. 18 and 19. Thus, these motions are essential in magnetotail physics.

The results of our numerical simulations demonstrate a good agreement with the so-called double-gradient (DG) model,[20,21] which allows us to investigate the model scope. Even though the DG model is not the only mechanism to explain flapping oscillations, recent case studies have shown that it may suggest the best *in-situ* data interpretation for some events.[22,23] A detailed discussion of the DG and other MHD[24–26] and kinetic[27–33] models of flapping oscillations is provided in our previous papers.[34,35] To avoid repetitions, here we just outline briefly the essential features of the DG model and its limitations.

The model was developed in Ref. 20 for a current sheet of length L and half-width Δ, where the magnetic component $B_x(z) \sim z$ for $|z| < \Delta$ is a linear function within the sheet, and is constant outside: $B_x = \pm B_0$ for $|z| > \Delta$, while B_z is a linear function of x. Here and throughout the paper, the x-axis points tailward from the Earth, the y-axis points dawnward, and the z-axis completes the righthanded system, as it is shown in Fig. 1. Considering long-periodic oscillations of the elongated current sheet ($\Delta/L = \nu \ll 1$) with a weak and slowly varying normal magnetic component ($\max(B_z)\Delta/\max(B_x)L = \epsilon \ll \nu$), the DG model predicts oscillations in the form of a plane wave $\sim \exp[i(ky-\omega t)]$, where the wavenumber k is the y-component of the wave vector $\mathbf{k} = (0,\,k,\,0)$. Two different types of initial perturbation $\delta V_z(z)$, odd and even, produce the waves of sausage type (lower frequencies) and kink type (higher frequencies), respectively.

In Ref. 21, the analytical solution was obtained also for a Harris-like current sheet ($B_x \sim \tanh(z/\Delta)$) with a small linear normal magnetic component $B_z(x)$. The analytical dispersion curve of the kink mode was derived in the following form:

$$\omega = \omega_f \sqrt{\frac{k\Delta}{k\Delta+1}}, \tag{1}$$

$$\omega_f = \sqrt{\left(\frac{1}{\mu_0 \rho}\frac{\partial B_x}{\partial z}\frac{\partial B_z}{\partial x}\right)_{z=0}}, \tag{2}$$

where μ_0 is the permeability of free space and ω_f is the typical frequency called "flapping frequency." The negative product of two magnetic gradients in Eq. (2) yields imaginary ω and, hence, the exponentially growing perturbations, i.e., instability. Vice versa, real ω corresponds to the wave propagating in $\pm y$ directions. Thus, for the DG mode, the sign of the derivative $\partial B_z/\partial x$ operates as a switch between stable/unstable regimes, the same as for many other modes,

---

[a)] Electronic mail: daniil.korovinskiy@oeaw.ac.at

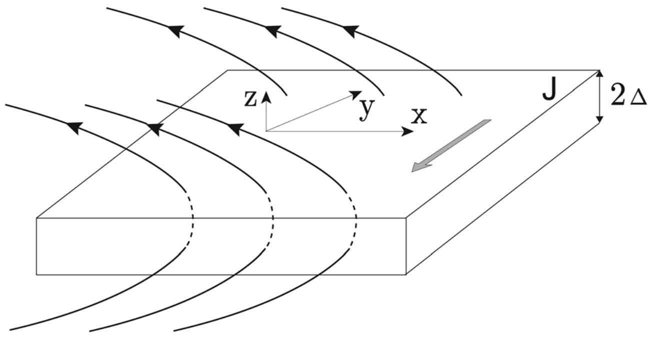

FIG. 1. Sketch of the background magnetic configuration in the magnetotail and the coordinate system as used in this paper. The Earth is to the left.

e.g., Refs. 26 and 36–43. Noteworthy, the dispersion relations (1) and (2) cover both stable and unstable modes. This resembles the Rayleigh–Taylor instability switching to the propagating wave, when heavy and light liquids swap places. It was also shown that a stable configuration should demonstrate a small gap of the total (gas + magnetic) pressure, Π, in the center of the sheet, while a central maximum of Π yields the unstable sheet.[20]

The simplicity and clearness of the DG model are achieved by a number of analytical limitations. The linearized MHD equations are solved for (a) incompressible plasma; (b) long-wavelength perturbations as compared to the field line curvature radius, $\lambda > R_c$; (c) the flapping frequency ω_f is assumed to be constant; and (d) perturbations are assumed to be independent of x. Thus, the model was developed in the frame of a quasi-one-dimensional approximation; hence, further verification is not redundant.

The model was tested by means of two-dimensional linearized MHD and three-dimensional full MHD simulations of the unstable kink mode, developing in a Harris-like current sheet[44] and at the Pritchett and Coroniti[41] background.[34,35] It is found out that numerical growth rates are close to the analytical prediction with $\omega_f = \max[\omega_f(x)]$ for 2D simulations and $\omega_f = \langle \omega_f(x) \rangle$ for 3D simulations, where angle brackets mean averaging. It was shown also that an instability does not evolve when curvature radius is too large ($R_c > L > \lambda$). The perturbations were found to be almost uniform on the x-coordinate, in support of the analytical assumptions.[34] Hence, the analytical limitations enumerated above are partly justified. However, several open questions remain and are addressed in the present paper: (a) Does the analytical model match the oscillating regime? (b) How much does compressibility contribute to the development of oscillations? (c) How close are perturbations to the analytical eigenfunctions? (d) How substantial is the contribution of term $\sim B_z$ neglected in the analytical solution?[21]

The paper is organized as follows: In Sec. II, we state the problem and analytical approach; the numerical method is described in Sec. III; results are presented in Sec. IV and discussed in Sec. V.

II. PROBLEM AND APPROACH

We study kink oscillations in a Harris-like current sheet with a small additional linearly varying normal magnetic component. Background magnetic field and plasma pressure are fixed as follows:

$$B_x = -\tanh(z), \tag{3}$$

$$B_z = A + Bx, \tag{4}$$

$$P = P_0 - \left(B + \frac{1}{\cosh^2(z)}\right)(Ax + 0.5Bx^2) - 0.5\tanh^2(z) - B\ln(\cosh(z)), \tag{5}$$

where $A = 0.1$, $B = -0.01$, and $P_0 = 5$. Mass density is assumed to be uniform, $\rho_0 = 1$. Here, the magnetic field components are normalized to the field value at "infinity," B_0; pressure to $B_0^2/(\mu_0)$; spatial variables are normalized to the sheet half-width Δ; and time to the Alfvén time Δ/V_A, where V_A is the Alfvén velocity.

Magnetic field lines and the total pressure Π for the background configuration are shown in Fig. 2. In the x-range $0 < x < 20$, $\Pi(x,z)$ demonstrates a minimum in the center of the sheet ($z = 0$) for any fixed value of x. However, $\Pi(x,0)$ is not uniform, the pressure gap deepens from the left to the right, reaching the lowest value (90% of P_0) at $x = 10$ and then flattens out again. In the ranges $x < 0$ and $x > 20$, $\Pi(x,z)$ has a bulge in the sheet center; hence, the configuration is unstable there. Thus, the region $0 < x < 20$ complies both analytical conditions of the wave mode: positive product of two magnetic gradients and central minimum of the total pressure.

The set of compressional ideal MHD equations[45] is solved numerically using the perturbation method. All variables are represented as a sum of two terms: the equilibrium state U_0 and a small perturbation U_1; hence, MHD equations are linearized. The solution U_1 is found in the form of a wave, propagating in y-direction within the current sheet: $U_1 = \delta U(x,z,t;k)\exp(iky)$, where the perturbation amplitude is $\delta U(x,z,t;k)$. Therefore, the system of linearized equations for amplitudes takes the conservative form

$$\frac{\partial(\delta\mathbf{U})}{\partial t} + \frac{\partial \mathbf{F}_x}{\partial x} + \frac{\partial \mathbf{F}_z}{\partial z} = \mathbf{S}, \tag{6}$$

where

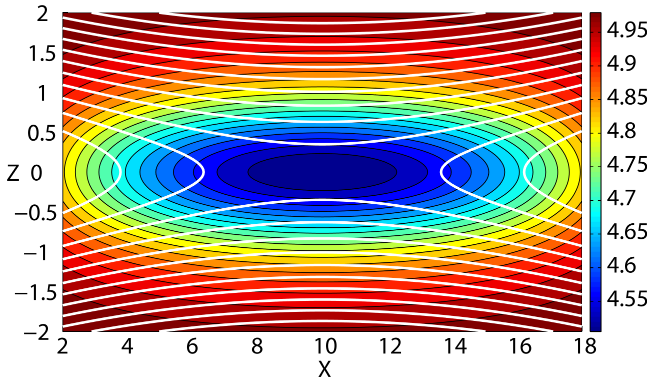

FIG. 2. Background configuration: white curves denote magnetic field lines. Total (gas + magnetic) pressure is shown by a color contour plot.

$$\delta\mathbf{U} = (\delta\rho, \{\delta M_i\}, \{\delta B_i\}, \delta E)_{i=x,y,z}. \tag{7}$$

The variable $\mathbf{U}$ denotes the vector of plasma parameters, where $M_i = \rho V_i$ is the momentum, $E = P/(\kappa - 1) + 0.5\rho V^2 + 0.5B^2$ is the total energy density, and κ is the polytropic index (the value of 5/3 is utilized if not otherwise stated). The expressions for the flux densities $\mathbf{F}_x$ and $\mathbf{F}_z$ and for the source function $\mathbf{S}$ are given in Appendix. These functions depend on the initial state $\mathbf{U}_0$, on perturbations $\delta\mathbf{U}$, on the wave number k, on coordinates x and z, but not on coordinate y. In this way, the initial full MHD system of equations is reduced to a time-dependent two-dimensional problem for complex quantities $\delta\mathbf{U}(x, z, t; k)$, where the physically meaningful quantities are $\Re[\delta\mathbf{U}\exp(iky)]$. Simulations are seeded with initial perturbation $\delta\mathbf{U}_0$. It is particularly convenient to initiate simulations with a perturbation of the normal component of the velocity, δV_{z0}. For real δV_{z0} and a background magnetic field component $B_y = 0$, this gives the set of eight non-zero physically meaningful functions: $\Re(\delta\rho)\cos(ky)$, $\Re(\delta M_x)\cos(ky)$, $\Im(\delta M_y)\sin(ky)$, $\Re(\delta M_z)\cos(ky)$, $\Re(\delta B_x)\cos(ky)$, $\Im(\delta B_y)\sin(ky)$, $\Re(\delta B_z)\cos(ky)$, $\Re(\delta E)\cos(ky)$.

Solving the system (6) for different values of the wavenumber k, we aim to obtain and investigate purely oscillating solutions with a frequency $\omega(k)$. While the exact analytical solutions of (6) cannot be derived, their estimations are provided by the DG model in the frame of a quasi-one-dimensional approximation and eigenmode analysis. These simplified solutions, presented below, form the basis for our approach to the problem.

For perturbations $\sim\exp[i(ky - \omega t)]$, the DG eigenfunctions of the problem are expressed via perturbations of the normal component of velocity, $\delta V_z(z; k)$

$$\delta\rho = 0, \tag{8}$$

$$\delta V_x = 0, \tag{9}$$

$$\delta V_y = \frac{i}{k}\frac{\partial\delta V_z}{\partial z}, \tag{10}$$

$$\delta B_x = -\frac{1}{\omega}\frac{\partial B_x}{\partial z}\delta V_z, \tag{11}$$

$$\delta B_y = \frac{i}{k\omega}B_z\frac{\partial^2\delta V_z}{\partial z^2}, \tag{12}$$

$$\delta B_z = \frac{1}{\omega}B_z\frac{\partial\delta V_z}{\partial z}, \tag{13}$$

$$\delta p = -\frac{\omega}{k^2}\rho_0\frac{\partial\delta V_z}{\partial z}. \tag{14}$$

Expressions (8)–(14) represent the solution of the system (11)–(15) in Ref. 21 for real δV_z and ω. Eigenfunctions δV_z, in their turn, are expressed via Legendre functions P_λ^μ (see Eq. (19), ibid.)

$$\delta V_z = P_\lambda^\mu[\tanh(z)], \tag{15}$$

$$\mu = -k, \tag{16}$$

$$\lambda = -\frac{1}{2} + \left[\frac{1}{4} + \left(\frac{k\omega_f}{\omega}\right)^2\right]^{1/2}. \tag{17}$$

For the kink mode, the parity condition requires $\lambda + \mu = 2m$ for $m = \{0, 1, 2, \ldots\}$. Here, quantities z, k, and ω are normalized, as stated above.

Thus, for any fixed value of the wavenumber k, one has an infinite set of decreasing eigenfrequencies $\omega_m(k)$ and corresponding eigenfunctions. For $m = 0$, Eq. (17) yields the dispersion relation (1) and (2), where the terms Δ and $1/\mu_0$ disappear due to normalization. Dispersion curves for $m = \{0, \ldots, 6\}$ are plotted in Fig. 3, and eigenfunctions $\delta V_z(z)$ for $k = 1$ and $m = \{0, 1, 2\}$ are shown in Fig. 4. For arbitrary initial perturbation $\sim\exp[iky]$, the general solution of the simplified time-dependent system (Eq. (10) in Ref. 21) takes the form $\delta\mathbf{U}(x, z, t; k) = \Sigma_{m=0}^{\infty}A_m(k)\delta\tilde{\mathbf{U}}_m(x, z; k)\exp[-i\omega_m(k)t]$, where $\delta\tilde{\mathbf{U}}_m$ are the vectors of eigenfunctions and coefficients A_m are to be found from an expansion of the initial perturbation. The solution may also be presented in the form of spectrum $H[\omega(k)]$, where the peaking frequency, ω_{peak}, and width, $2\Delta\omega$, depend on the initial perturbation. When the initial perturbation is given by the m-th set of eigenfunctions (8)–(15), the spectrum has the single line at $\omega_m(k)$.

Generally speaking, these analytical results do not span the true solution of the system (6). However, when the current sheet parameters satisfy the DG model assumptions, we suppose that DG estimates resemble the true solution with a good accuracy. This means that if we initiate the evolution of the sheet parameters with perturbations which are close to the m-th set of eigenfunctions (8)–(15), we may expect that after a transitional process, the solution of Eq. (6) does converge to oscillations with a frequency close to the m-th eigenfrequency of Eq. (17). Hence, the solution spectrum $H[\omega(k)]$ is supposed to have a pronounced peaking frequency, $\omega_{peak}(k)$, close to $\omega_m(k)$. The difference between obtained values $\omega_{peak}(k)$ and $\omega_m(k)$ quantifies the inaccuracy of the DG model approach and predictions. In the current paper, we use the zeroth mode of the solution (8)–(15) to achieve the oscillating solution of the system (6). The obtained dispersion curve is found to be rather close to the highest branch of the analytical dispersion curve, $\omega_0(k)$,

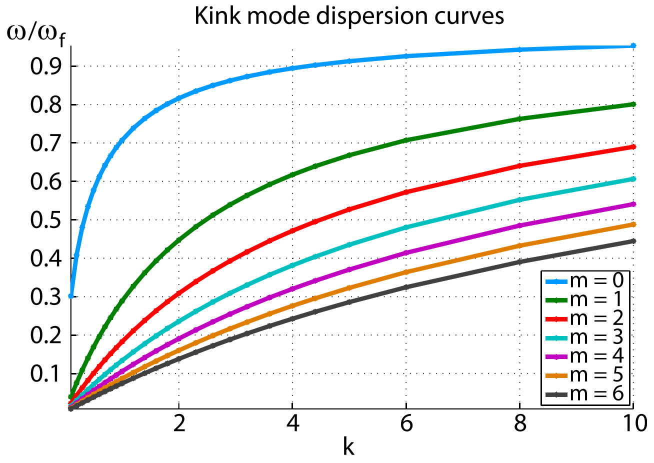

FIG. 3. Normalized dispersion curves $\omega(k)/\omega_f$ of kink oscillations, calculated from Eq. (17), where $\lambda - k = 2m$, are plotted for $m = 0$ (blue), for $m = 1$ (green), for $m = 2$ (red), for $m = 3$ (cyan), for $m = 4$ (violet), for $m = 5$ (orange), and for $m = 6$ (black).

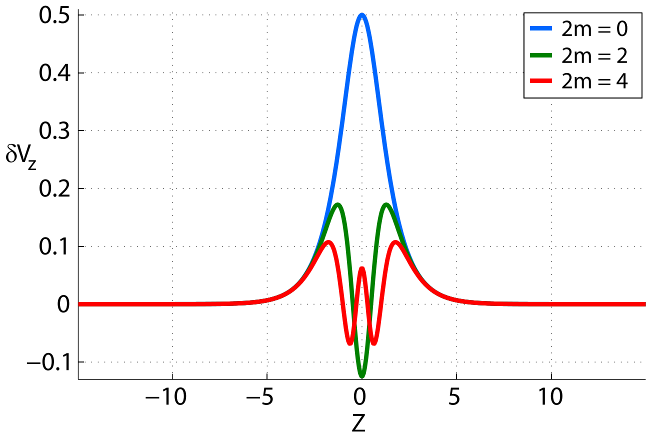

FIG. 4. Analytical eigenfunctions $\delta V_z(z)$, calculated from Eq. (15), where $\lambda+\mu=2m$ and $\mu=-k=-1$, are plotted for $m=0$ (blue), for $m=1$ (green), and for $m=2$ (red).

given in Eqs. (1) and (2), and shown by the blue curve in Fig. 3.

III. METHOD

Equations (6) are solved numerically by means of the 3rd order central semi-discrete upwind scheme[46] with open boundary conditions $\partial/\partial\mathbf{n}=0$. Semi-discrete schemes allow any appropriate ordinary differential equation (ODE) solver to be used for time integration of the equations for cell averages. In the simulations below, we have used the optimal (in the sense of Courant–Friedrichs–Lewy (CFL) coefficient and the computational cost) strong stability preserving Runge–Kutta method of the 3rd order described in Ref. 47. The integration time step (CFL number $=0.5$) is adopted to ensure the convergence of the results with respect to values of the time step. The $(\nabla\cdot\mathbf{B})=0$ constraint is enforced on each time step using the method of projection.[48]

To initiate oscillations, two types of initial perturbations are used. The first one is the Gaussian perturbation $\delta V_{z0}=\exp(-z^2)$, resembling the analytical eigenfunction $V_z(z)$ by Eq. (15) for $m=0$, shown in Fig. 4 by the blue curve. Another one represents a full set of analytical eigenfunctions (8)–(15) for $m=0$, shown in Fig. 5 for $k=\{0.5,\ 1,\ 2\}$. The approximate solution (8)–(15) does not match exactly the eigenfunctions of the two-dimensional problem under consideration; however, it is closer than the single Gaussian perturbation of V_z. Therefore, the numerical solution reaches the oscillating regime more quickly if analytical eigenfunctions rather than Gaussian perturbation of V_z are used to initialize the evolution of (6). In both cases, we observe that after some transitional process, the solution converges to damped harmonic oscillations with a frequency close to the prediction of the DG model. The damping of oscillations is related to numerical dissipation (that can be decreased by reduction of the mesh steps) and to the use of open boundary conditions.

The remnants of transitional processes and the attenuation of oscillations due to numerical damping lead to an inaccuracy of the results. Namely, for any fixed k, instead of a single spectrum, oscillations are characterized by spectrum curves $H_j(\omega)$, which are calculated individually for each quantity using fast Fourier transform. The more accurate the numerical solution is, the more exact the spectra $H_j(\omega)$ coincide. The spectra widths $2\Delta\omega_j(k)$ estimate the "quality" of the DG approximation for a given parameters of the current sheet, though additional spectral broadening results from the numerical dissipation.

These transitional and numerical effects complicate the accurate analysis of the numerically obtained spectra $H_j(\omega)$. However, when the DG model assumptions are fulfilled, the spectra turn out to be narrow enough, and peaking frequencies $\tilde{\omega}_{peak,j}$ coincide to a high accuracy. The symbol "tilde" is used here to separate the true eigenfrequency $\omega(k)$ and its approximate estimate by numerical simulations, $\tilde{\omega}_j(k)$. Therefore, we have used a simple approach to estimate the frequency of oscillations. Namely, when the numerical

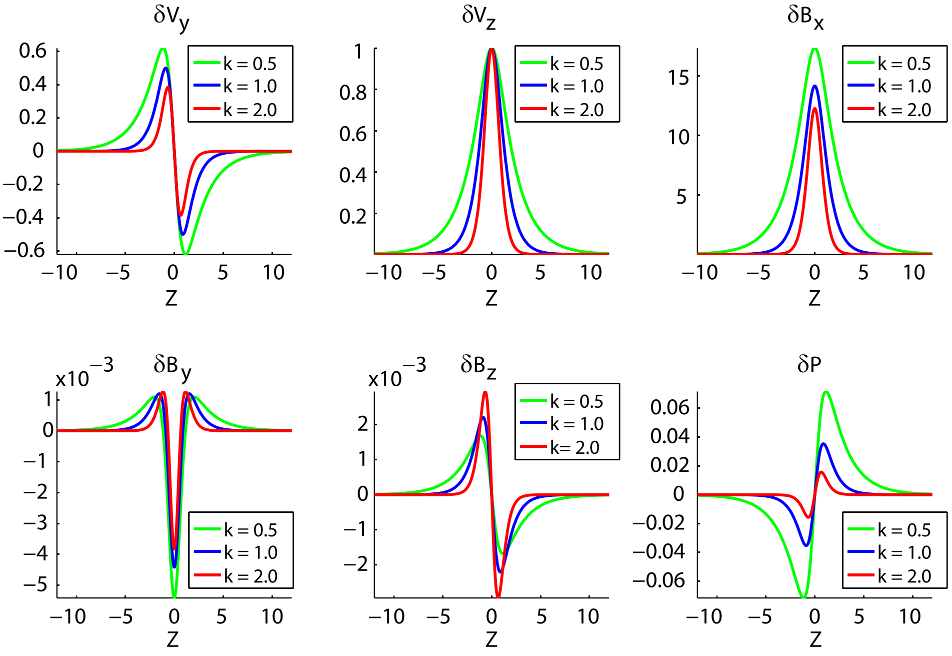

FIG. 5. Analytical eigenfunctions (10)–(15), where $\lambda+\mu=0$, are plotted for wavenumber values $k=0.5$ (green), $k=1$ (blue), and $k=2$ (red) at $x_0=10-1/2^5$. Normalization: $\max(|\delta V_z|)=1$.

solution of the system (6) for some fixed value of k is obtained, the frequency of oscillations is computed at one point in the center of the sheet by fitting the quantities $\Re[\delta\rho(t)]$, $\Re[\delta V_x(t)]$, $\Im[\delta V_y(t)]$, $\Re[\delta V_z(t)]$, $\Re[\delta B_x(t)]$, $\Im[\delta B_y(t)]$, $\Re[\delta B_z(t)]$, $\Re[\delta E(t)]$ with the functions

$$f_j(t) = a_j \exp(\gamma_j t)\sin(\tilde{\omega}_j t + \phi_{0j}), \quad j = \{1, 2, ..., 8\}. \tag{18}$$

Then, the value of the eigenfrequency ω is estimated by averaging $\tilde{\omega} = \langle\tilde{\omega}_j\rangle \pm \sigma_\omega$. The standard deviation σ_ω quantifies the average width of spectra $H_j(\omega)$. Numerical attenuation of oscillations is quantified by negative γ_j.

The numerical results were tested for sensitivity to the box crosswise size and mesh step. In Fig. 6, the wave frequency $\tilde{\omega}$, calculated at the point ($x_0 = 10 - 1/2^5$, $z_0 = -1/2^5$), is plotted for three values of the wavenumber $k = \{0.1, 1, 10\}$ for different values of the computational box boundary location z_{max}. It is seen that for any value of k, we can place the z-boundary far enough to make the results independent of the boundary location. The lower the wavenumber, the wider should the computational box be, and vice versa. This is due to the fast broadening of the eigenfunctions' profiles across the sheet with decreasing value of k, as it is seen in Fig. 5.

The dependence of $\tilde{\omega}$ on the mesh step $dx = dz = 1/2^n$, where $n = \{2, 3, 4, 5, 6\}$, is shown in Fig. 7. It is seen that for a small values of k ($\sim$1 or less), we can consider $n = 4$ as the maximal required grid refinement. For $1 < k < 5$, $n = 5$ seems to be enough, while for $k > 5$, the furthermost refinement is eligible. However, with the value $n = 4$, one can expect the error within 10% or less for any $k \in [0, 10]$.

Fig. 8 depicts the decrement of oscillations $\gamma = \langle\gamma_j\rangle \pm \sigma_\gamma$, where γ_j are calculated by Eq. (18), as a function of wave number (black curve), mesh step (colored asterisks), and polytropic index κ (colored crosses). It is seen that the attenuation of oscillations is slower for longer wavelengths and thinner grids. This looks reasonable for pure numerical effect, as a decrease of the wavelength is equivalent to an increase in the mesh step. Conformably, reduction of the mesh step reduces numerical damping.

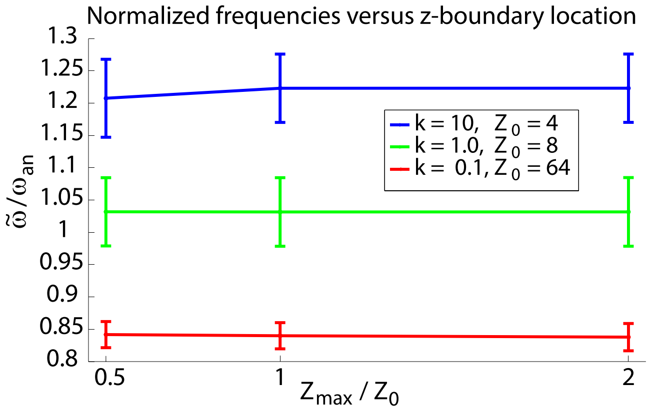

FIG. 6. Wave frequencies $\tilde{\omega} = \langle\tilde{\omega}\rangle \pm \sigma_\omega$, normalized to the analytically predicted values (1), are calculated in the point ($x_0 = 10 - dx/2$, $z_0 = -dz/2$) and shown as functions of the z boundary location z_{max} for wavenumbers $k = 10$ (blue), $k = 1$ (green), and $k = 0.1$ (red). Simulations are performed in the box $[6, 14] \times [-z_{max}, z_{max}]$ with mesh step $dx = dz = 1/2^4$. The values of z_{max} are normalized to $z_0 = 64$ for $k = 0.1$, to $z_0 = 8$ for $k = 1$, and to $z_0 = 4$ for $k = 10$.

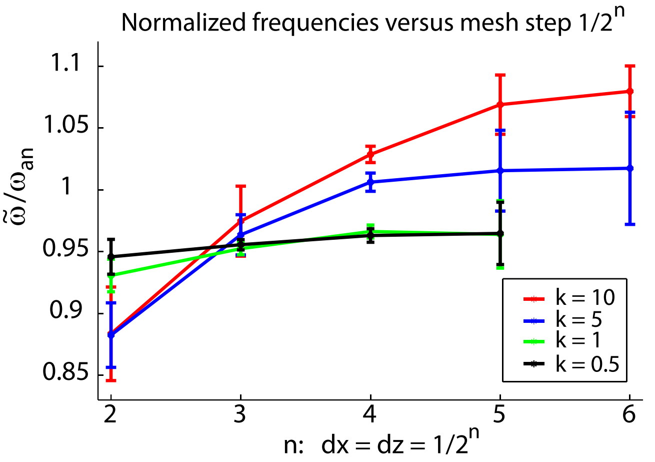

FIG. 7. Wave frequencies $\tilde{\omega} = \langle\tilde{\omega}\rangle \pm \sigma_\omega$, normalized to the analytically predicted values (1), are calculated at the point ($x_0 = 10 - dx/2$, $z_0 = -dz/2$) and shown as functions of the mesh step $dx = dz = 1/2^n$ for wavenumbers $k = 10$ (red), $k = 5$ (blue), $k = 1$ (green), and $k = 0.5$ (black). Simulations are carried out in the x-range [9, 11].

In the incompressible limit $\kappa \to \infty$, the decrement indicates a trend to negligible values. This means that open boundary conditions do not prevent energy outflow carried away by acoustic mode. Comparison of the numerically obtained frequencies with analytical estimates, presented in Section IV, shows that the effect of these energy losses is minor. Besides, the projection procedure used to enforce the $(\nabla \cdot \mathbf{B}) = 0$ condition also introduces some amount of dissipation into the numerical scheme.

At the same time, a simple approach adopted in the current paper leaves out all physical mechanisms of the oscillations' damping. In the frame of an ideal MHD, several such mechanisms may be reported. In Ref. 49, it was shown that oscillations may lose their energy in short time (few periods)

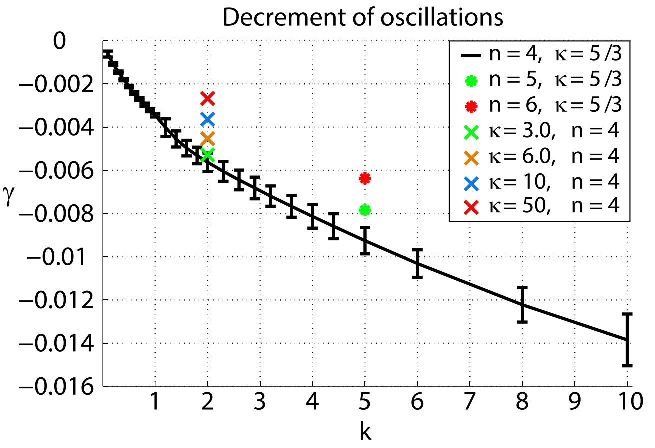

FIG. 8. Black curve: decrement of oscillations $\gamma = \langle\gamma_j\rangle \pm \sigma_\gamma$ as a function of wavenumber k for polytropic index $\kappa = 5/3$ and mesh step $dx = dz = 1/2^n$ for $n = 4$. Colored asterisks show the decrement as function of the mesh step for $k = 5$, $\kappa = 5/3$, $n = 5$ (green), and $n = 6$ (red). Colored crosses depict the decrement as a function of κ for wavenumber $k = 2$ and mesh step $1/2^4$ for $\kappa = 3$ (green), $\kappa = 6$ (orange), $\kappa = 10$ (blue), and $\kappa = 50$ (red). Calculations are carried out in the x-range [9, 11]; the decrement is calculated at the point $(10 - dx/2, -dz/2)$.

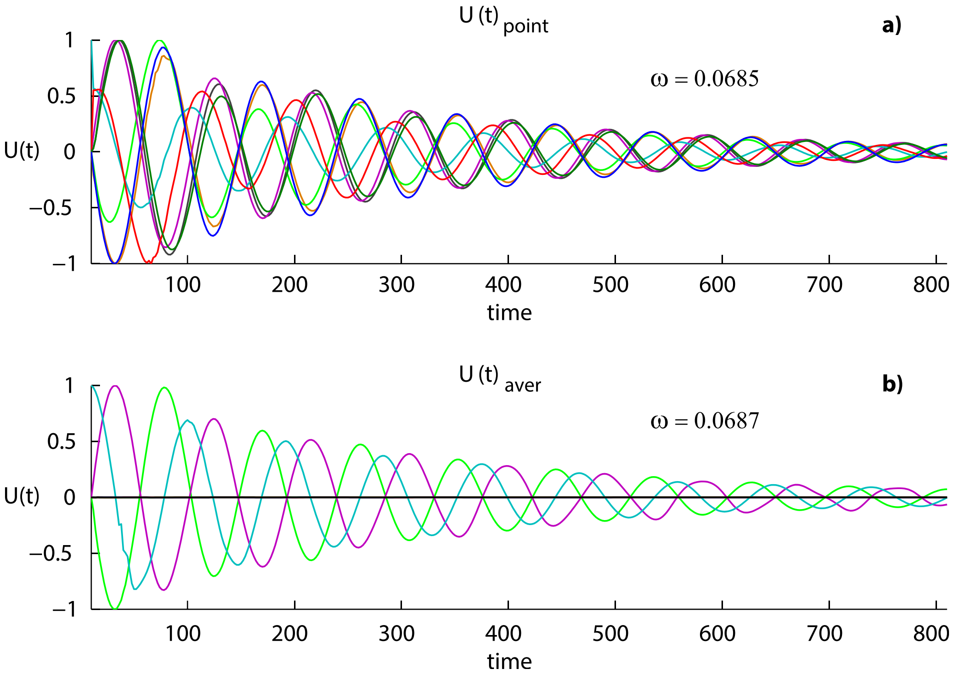

FIG. 9. Solution of the system (6) $\delta\mathbf{U}(t)$ for $k = 1$ is found in the box $[x \times z] = [9, 11] \times [-64, 64]$ with mesh step $dx = dz = 1/2^4$. Simulations are seeded with $\delta V_{z0} = \exp(-z^2)$. Top panel: Normalized quantities $\Re(\delta\rho)$ (blue), $\Re(\delta V_x)$ (dark green), $\Im(\delta V_y)$ (red), $\Re(\delta V_z)$ (cyan), $\Re(\delta B_x)$ (magenta), $\Im(\delta B_y)$ (light green), $\Re(\delta B_z)$ (black), and $\Re(\delta E)$ (orange) versus time at the point $(10 - dx/2, -dz/2)$. In the bottom panel, the values averaged across the sheet at the cross-section $x_0 = 10 - dx/2$ are shown.

due to the interaction with the ionosphere. Three-dimensional MHD simulations[34] reveal that the flapping frequency is a non-local quantity, which can be affected by changes in remote parts of the current sheet. Furthermore, in Ref. 50, it was demonstrated that in thin current sheets, the Hall effect may suppress the DG mode in the direction opposite to the current.

IV. RESULTS

A series of simulations is carried out in the x-range [9, 11], covering the deepest total pressure minimum at $x = 10$, where the background magnetic component $|B_z| \le 0.01$. In this region, the problem demonstrates the best resemblance to the quasi-one-dimensional analytical model; hence, the best agreement of the results may be expected.

Fig. 9 shows the sample solution obtained in the box $[x \times z] = [9, 11] \times [-64, 64]$ with mesh step $dx = dz = 1/2^4$ for $k = 1$. Normalized quantities $\Re(\delta\rho)$ (blue), $\Re(\delta V_x)$ (dark green), $\Im(\delta V_y)$ (red), $\Re(\delta V_z)$ (cyan), $\Re(\delta B_x)$ (magenta), $\Im(\delta B_y)$ (light green), $\Re(\delta B_z)$ (black), and $\Re(\delta E)$ (orange) are plotted in the top panel versus time in the point $(10 - dx/2, -dz/2)$. In the bottom panel, the values averaged across the sheet at the cross-section $x_0 = 10 - dx/2$ are shown. It is seen that the frequency of the sheet oscillations, $\tilde{\omega}_{aver} = 0.0687$, is almost the same to the frequency measured in the central point, $\tilde{\omega}_{point} = 0.0685$. This means that the entire current sheet oscillates with the same frequency, and oscillations may be registered far enough from the sheet center. The transitional process from initial configuration to the oscillatory solution is seen in the plots of δV_y, δV_z, and δE at time $t < 100$.

The dispersion curves of the kink mode, shown in Fig. 10, are calculated in the same box for two types of initial perturbation: eigenfunctions (8)–(15) for all quantities (red), or single $\delta V_{z0} = \exp(-z^2)$ (blue). Blue points lay almost exactly on the red curve, confirming that the result does not depend on the type of initial perturbation if it bears a resemblance to the zeroth mode eigenfunctions.

One can also see that the standard deviation increases with growing k values, meaning that the spectra broadened, as it is shown in Fig. 11. The Fourier spectra half-width $\Delta\tilde{\omega}$ may be estimated as 0.015 for $k = 0.4$, 0.03 for $k = 2$, and 0.05 for $k = 10$. In normalized units $\Delta\tilde{\omega}/\tilde{\omega}_{peak}$, this gives $\approx\{0.3, 0.4, 0.5\}$, respectively. Fig. 11 illustrates that for small and moderate wavenumbers, the value $\tilde{\omega}_{peak}$ is the same for all eight quantities. For high k, values $\tilde{\omega}_{peak,j}$ start to diverge, meaning that the accuracy of the numerical solution diminishes due to the high numerical dissipation.

Growth of $\Delta\tilde{\omega}$ with growing wavenumber k means that the analytical solution (8)–(15) deviates more and more from the true solution of the problem (6). This is demonstrated in

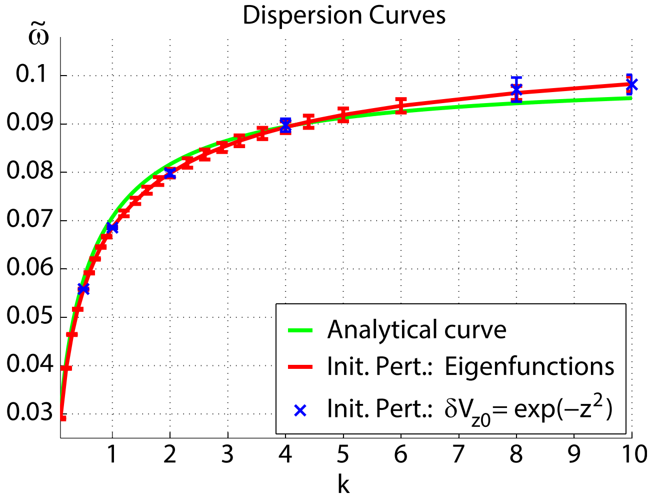

FIG. 10. Numerical dispersion curves $\tilde{\omega}(k)$ are plotted for two types of initial perturbation: eigenfunctions (8)–(15) (red) and single $\delta V_{z0} = \exp(-z^2)$ (blue). The analytical prediction (1) is shown by the green curve. Simulations are performed in the box $[x \times z] = [9, 11] \times [-64, 64]$ with mesh step $1/2^4$.

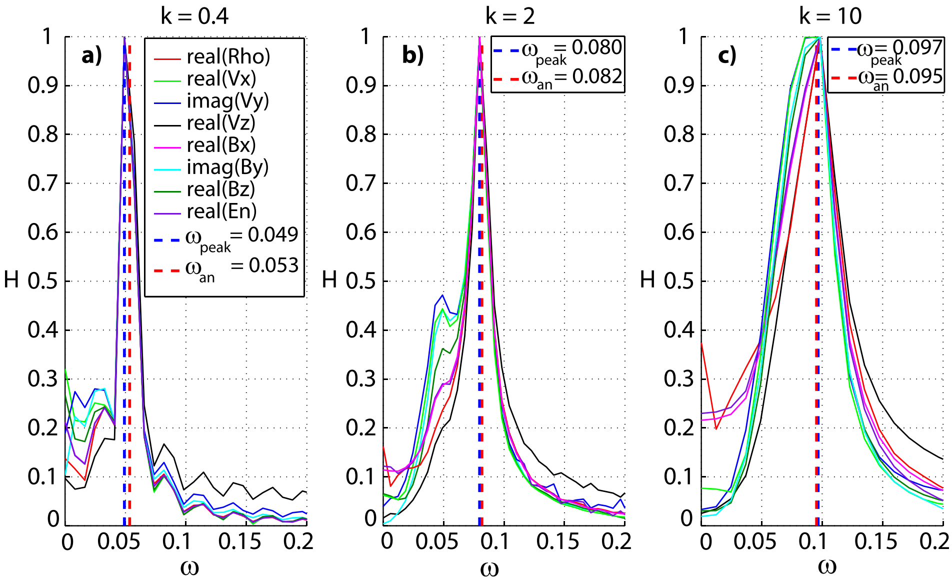

FIG. 11. Normalized Fourier spectra $H_j(\omega)$ of oscillations at the point $(x_0 = 10 - dx/2,\ z_0 = -dz/2)$ for wavenumber $k = 0.4$ (left), $k = 2$ (central), and $k = 10$ (right). Simulations are performed in the box $[9, 11] \times [-64, 64]$ with mesh step $1/2^4$ and $\delta V_{z0} = \exp(-z^2)$. Peaking frequencies are shown by dashed blue lines, analytical predictions by dashed red lines.

Figs. 12(a) and 12(b), where analytical eigenfunctions $\delta V_z(z;k)$ by Eq. (15) are compared to the numerical solutions obtained in runs initiated with eigenfunctions (8)–(15) and with $\delta V_{z0} = \exp(-z^2)$ for $k = 1$ and $k = 10$, respectively. For $k = 1$, both numerical curves match the analytical prediction (15) and each other (a small discrepancy indicates the numerical solution inaccuracy). For $k = 10$, curves match each other mainly, deviating from the analytical profile (considerable discrepancy reveals the inaccuracy of the analytical solution).

The numerical dispersion curves of Fig. 10 (red, blue) demonstrate a systematical overshoot of the analytical prediction (green) for $k > 4$ and undershoot for smaller k values. It turns out that the difference between numerical and analytical solutions displays the contribution of the plasma compressibility, which was neglected in the analytical model, but kept in the numerical one. In Fig. 13, frequencies $\tilde{\omega} = \langle \tilde{\omega}_j \rangle \pm \sigma_\omega$, normalized to the corresponding analytical values, are shown as functions of the polytropic index κ for wavenumbers $k = 10$ (red) and $k = 2$ (blue). Fitting curves are $f_1 = 1/\{1 - \exp[-2.42(\lg\kappa + 1)^{1/3}]\}$ and $f_2 = \tanh\{1.44\lg[17 + 4.72\kappa]\}$, respectively. It is seen that numerical values tend to analytical predictions in the incompressible ($\kappa \to \infty$) limit in both cases.

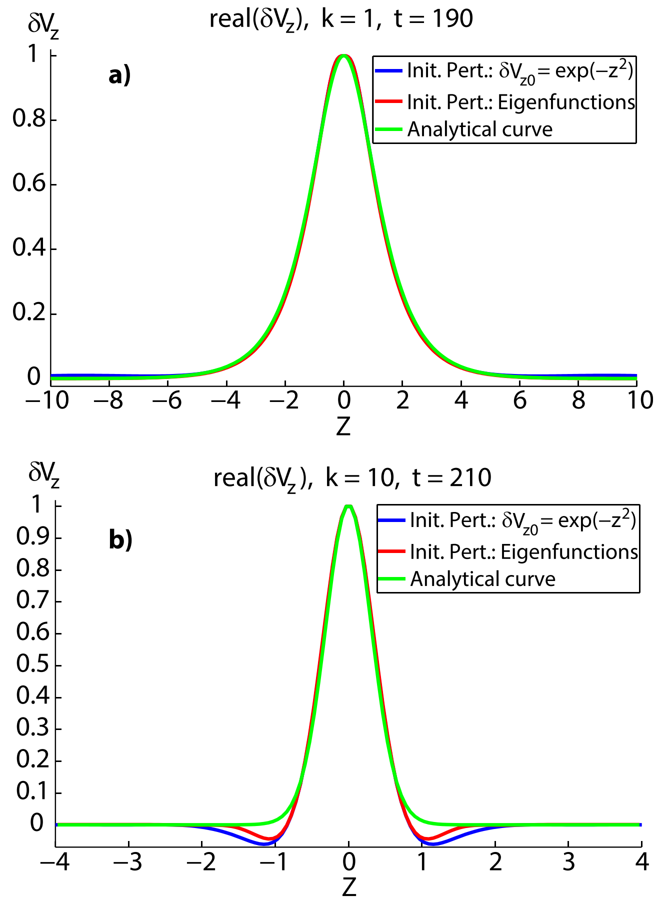

FIG. 12. At the upper panel, profiles of $\Re\{\delta V_z(z, x_0 = 10 - dx/2)\}$ for wavenumber $k = 1$ are shown for two runs: one initiated with $\delta V_{z0} = \exp(-z^2)$ (blue); another run initiated with eigenfunctions (8)–(15) (red). The green curve depicts the analytical solution (15). Normalization: $\max(|\delta V_z|) = 1$. At the lower panel, the same curves are shown for $k = 10$.

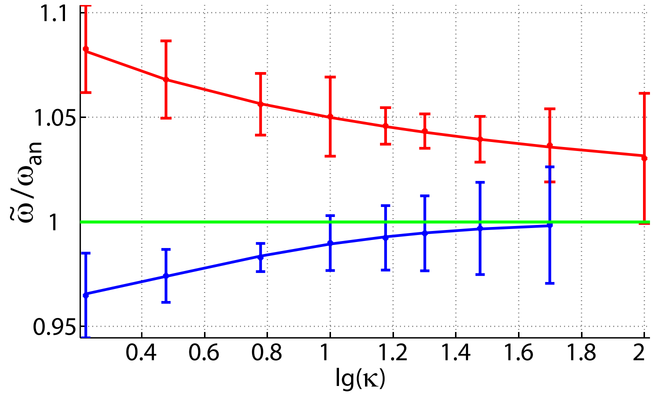

FIG. 13. Frequencies of oscillations, normalized to corresponding analytical values, are shown as functions of the polytropic index κ for wavenumber $k = 10$ (red) and $k = 2$ (blue). Fitting curves are $f_1 = 1/\{1 - \exp[-2.42(\lg\kappa + 1)^{1/3}]\}$ and $f_2 = \tanh\{1.44\lg[17 + 4.72\kappa]\}$, respectively. The red curve is computed in the box $[9, 11] \times [-4, 4]$ with mesh step $n = 1/2^5$; the blue curve is computed in the box $[9, 11] \times [-8, 8]$ with mesh step $n = 1/2^4$. Polytropic index $\kappa = \{5/3, 3, 6, 10, 15, 20, 30, 50, 100\}$.

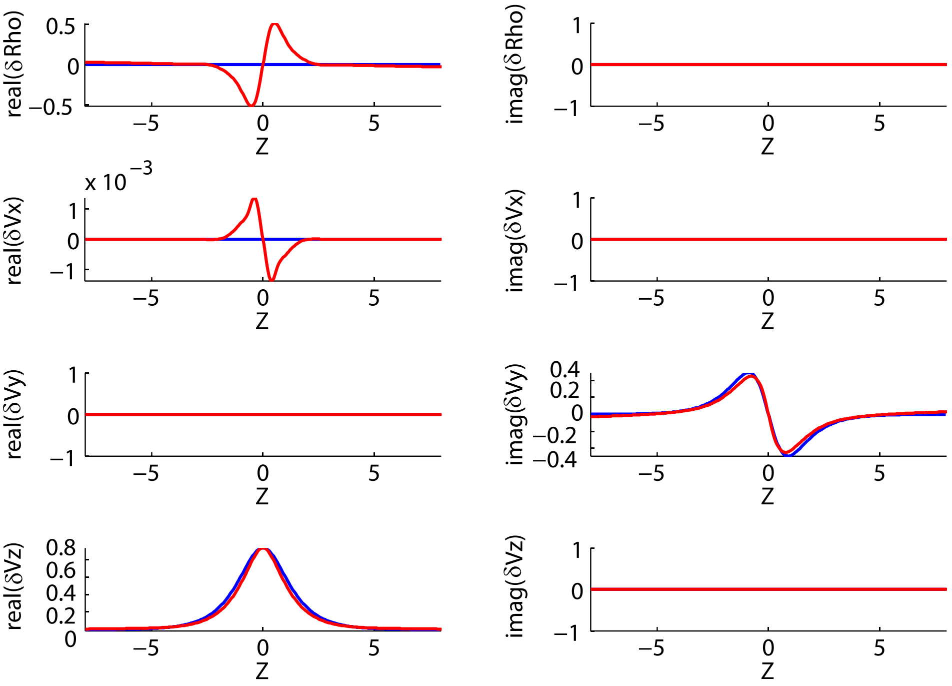

FIG. 14. Profiles of the analytically predicted (blue) and numerically computed (red) zeroth mode perturbations $\{\delta\rho,\ \delta V_x,\ \delta V_y,\ \delta V_z\}$ are plotted for wavenumber $k = 1$ at $x_0 = 10 - dx/2$ and time $t = 200$. Normalization: $\max(|\delta V_z|) = 1$, initial perturbation $\delta V_{z0} = \exp(-z^2)$, simulation box $[9,\ 11] \times [-64,\ 64]$, and mesh step $1/2^4$.

The calculated perturbations are compared to the analytical predictions (8)–(15) in Figs. 14 and 15. Profiles of perturbations are computed for the wavenumber $k = 1$ at $x_0 = 10 - 1/2^5$ for time $t = 200$. Perturbations and analytical quantities are normalized to the $\max(|\delta V_z|)$. It is seen that perturbations of velocity components V_y and V_z demonstrate brilliant agreement, meaning that the divergence-free equation $\cancel{\partial\delta V_x/\partial x} + \partial\delta V_y/\partial y + \partial\delta V_z/\partial z = 0$ used in Eq. (10) of the work[21] is fulfilled to a high accuracy. Indeed, the perturbation of V_x is found to be really weak (the analytical prediction is zero), contrary to the perturbation of the mass density, which turns out to be comparable with δV_z. Perturbations of magnetic components B_x and B_y demonstrate a good agreement with the analytical predictions in amplitude. The perturbation δB_z overshoots the theoretical quantity two times and the energy perturbation occurs two times lower than the analytical estimate, which should be accounted for the contribution of the mass density variation.

To estimate the contribution of the terms $\sim B_z$ neglected in the analytical model,[21] we ran simulations in the x-range $[1,\ 9]$, where $\max(B_z)$ reaches the value of 0.09, so that the analytical scaling assumptions fail. Fig. 16 demonstrates the normalized Fourier spectra for $k = 1$, calculated in the center of the sheet $z_0 = -dz/2$ at $x_0 = \{10,\ 8,\ 6,\ 4\} - dx/2$. It is

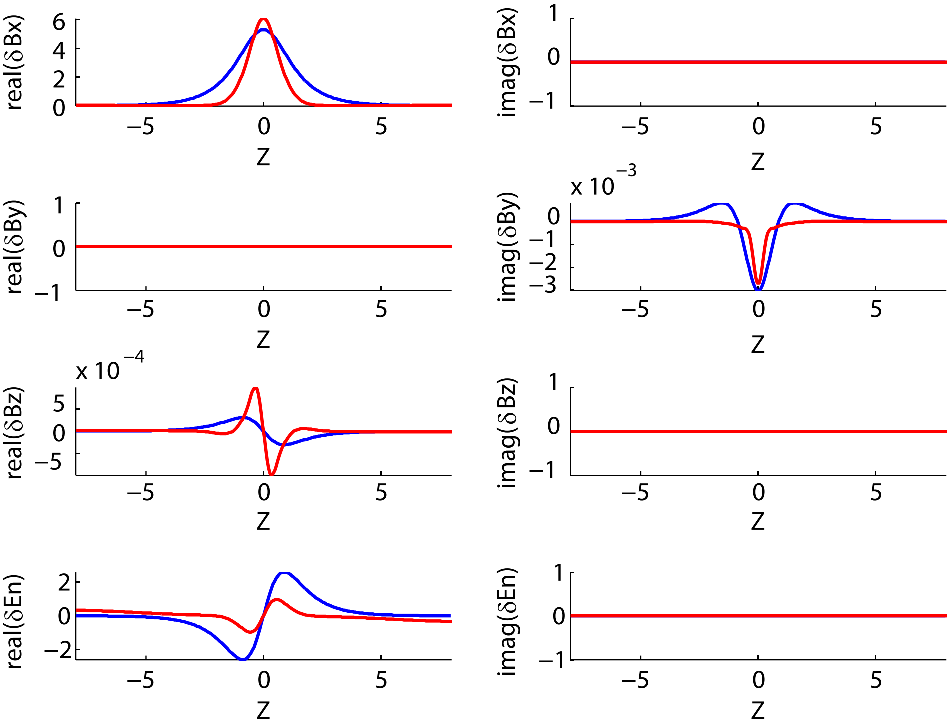

FIG. 15. Profiles of the analytically predicted (blue) and numerically computed (red) zeroth mode perturbations $\{\delta B_x,\ \delta B_y,\ \delta B_z,\ \delta E\}$ are plotted for wavenumber $k = 1$ at $x_0 = 10 - dx/2$ and time $t = 200$. Normalization: $\max(|\delta V_z|) = 1$, initial perturbation $\delta V_{z0} = \exp(-z^2)$, simulation box $[9,\ 11] \times [-64,\ 64]$, and mesh step $1/2^4$.

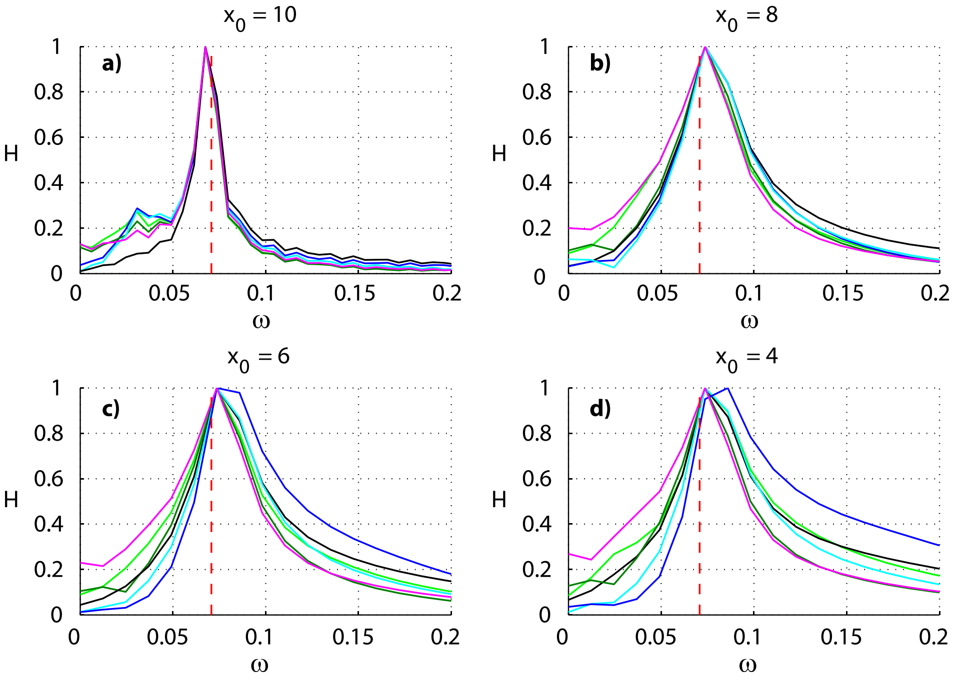

FIG. 16. Normalized Fourier spectra $H_j(\omega)/\max(H_j)$ of oscillations for wavenumber $k = 1$ are calculated at the sheet center ($z_0 = -1/2^5$) at $x_0 = 10 - dx/2$ (top, left), $x_0 = 8 - dx/2$ (top, right), $x_0 = 6 - dx/2$ (bottom, left), and $x_0 = 4 - dx/2$ (bottom, right). Simulations are seeded with eigenfunctions (8)–(15) and carried out in the range $x \in [9, 11]$ for the top left picture and $x \in [1, 9]$ for others. Mesh step $dx = dz = 1/2^4$. The analytically predicted frequency is plotted by dashed red lines. Labels of the curves are given in the legend of Fig. 11.

seen that with increasing distance from the sheet center ($x = 10$), where $B_z = 0$, spectra broaden more and more. For $x_0 = 4$, the normalized spectra half-width $\Delta\tilde{\omega}/\tilde{\omega}_{peak}$ reaches the value of 1. Corresponding profiles of $\Re[\delta V_z(z, x = x_0)]$ are shown in Fig. 17. With decreasing value of x_0 (growing B_z), the function $\delta V_z(z)$ deviates more and more from the analytical profile. This result makes the major difference with simulations of the DG instability, where perturbation profiles were found almost uniform on x.[34]

V. DISCUSSION AND CONCLUSIONS

In this paper, we have investigated long-wavelength kink-like waves propagating within the magnetotail current sheet in transversal direction. Oscillations of that type resemble well-known flapping oscillations. The system of two-dimensional time-dependent linearized MHD equations is solved numerically to calculate perturbations of a Harris-like current sheet with a small additional normal magnetic component $B_z(x)$, decreasing in the tailward direction.

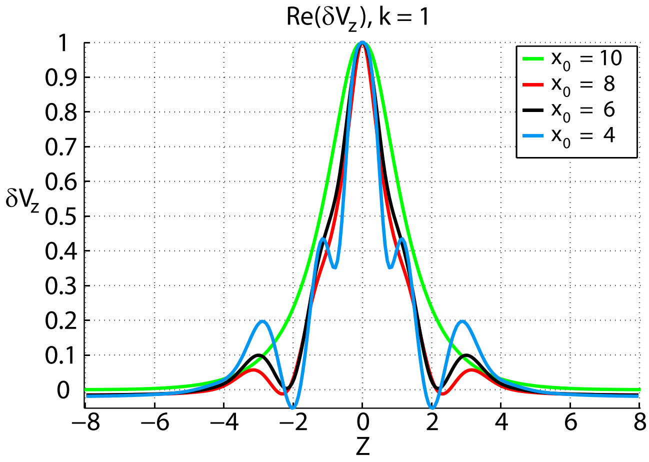

FIG. 17. Normalized profiles of $\delta V_z(z)$ for wavenumber $k = 1$ are plotted in the cross-sections $x_0 = 10 - dx/2$ (green), $x_0 = 8 - dx/2$ (red), $x_0 = 6 - dx/2$ (black), and $x_0 = 4 - dx/2$ (blue). Simulations are seeded with eigenfunctions (8)–(15) and carried out in the range $x \in [9, 11]$ for the green curve and $x \in [1, 9]$ for others. Mesh step $dx = dz = 1/2^4$.

Numerical simulations reveal that the analytical DG model[21] provides a reliable solution, when the current sheet parameters satisfy the model assumptions. It was shown previously that this requirement can be fulfilled in the Earth magnetotail.[51] It turns out that the most severe limitation of the DG model is the requirement of a small normal magnetic field component. As can be seen from Figs. 16 and 17, we may estimate the crucial value of B_z for our particular configuration as $0.05\,B_0$, where B_0 is the lobe magnetic field ($\sim 20\,$nT during the substorm growth phase[52,53]). At higher values of B_z, the analytical profiles of perturbations mismatch the numerical solution, while the half-width of the Fourier spectra of perturbations, $\Delta\tilde{\omega}$, exceeds the peaking frequency $\tilde{\omega}_{peak}$. Nevertheless, the value of $\tilde{\omega}_{peak}$ stays close to the DG model prediction.

Thus, while kink-type low-frequency (flapping) oscillations may exist even in current sheets with higher values of B_z, the DG model may provide only estimates of their frequencies, but not the profiles of perturbations. This means that the accuracy of the analytical solution for perturbations falls down with growing absolute value of B_z, while estimates of the typical frequency of oscillations stay accurate. The latter depends on the basic properties of the current sheet configuration (product of two magnetic gradients and minimum of total pressure). In our particular configuration, the product of magnetic gradients does not change with growing B_z, while total pressure minimum is preserved in interval $x \in (0, 20)$; hence, the low dependence of the frequency estimates accuracy on $|B_z|$.

At the same time, configurations with B_z below $1 - 2\,$nT are commonly found in THEMIS observations,[53] prior to substorm onset near midnight at distances $\sim 11\,Re$. When B_z is small, the DG model predictions demonstrate very good agreement with the numerical solution. The analytical dispersion curve matches the numerical one with the accuracy up to several percents (see Fig. 10). Simulations with increased value of polytropic index reveal that this minor discrepancy can be explained by plasma compressibility, neglected in the analytical model. Hence, this limitation of the model is found to be not crucial. This supports the conclusion made in Ref. 51, claiming that compressibility may be neglected in studies of low-frequency oscillations $\omega/(kc_s) \ll 1$, where c_s is the sound speed ($c_s \approx 3$ in our simulations with polytropic index $\kappa = 5/3$).

Then, the condition $1/R_c > k > 1/L$ is satisfied in our simulations for any $k \in [0.1, 10]$, as far as $R_c = |B_z/(\partial B_x/\partial z)|_{z=0} = |B_z|$ and $L \sim |\max(B_z)/(\partial B_z/\partial x)| \sim 10$. However, with growing value of k, the difference between analytical and numerical values of ω increases, and Fourier spectra of perturbations, shown in Fig. 11, broaden gradually. This is in accordance with our previous findings,[34] stating that the magnetic field line curvature radius is a lower limit for the DG mode wavelength.

A comparison of perturbation profiles with analytical eigenfunctions (Figs. 14 and 15) demonstrates an excellent agreement for quantities δV_y and δV_z, a good agreement for δB_x, and δB_y, and a qualitative agreement for δB_z and δE. This represents the contribution of the underlined terms of Eq. (10) in Ref. 21, which were neglected in an analytical solution. Noteworthy, the relative magnitude of perturbation δV_x amounts to $\sim 10^{-3}$. Taking into consideration the relative phase shift $\delta\phi = 111^\circ$ between δV_z and δV_x, calculated by Eq. (18), we obtain $\max|\delta V_x| \approx 3 \times 10^{-3}$, which is much less than $\max|\delta V_z| = 1$; hence, no plasma motion in the x-direction is found.

Summing up, linearized MHD simulations are found to be a handy tool for studying flapping oscillations in the current sheets with varying B_z component. When the latter is small enough, the analytical DG model provides accurate theoretical estimates. Essentially, dispersion curves of oscillations, obtained here, and the corresponding instability, studied in Ref. 44, are close to the same analytical prediction (1) and (2). This supports the wave generation mechanism suggested in Ref. 54. It assumes that the initial perturbation is produced by an instability, developing in the current sheet with tailward growing B_z. When $\partial B_z/\partial x$ changes its sign, the instability switches to the propagating flapping wave. The unique dispersion relation for stable/unstable regimes on the one hand and the frequent change of the B_z growth direction in the midtail[55] on the other hand make this scenario probable.

In our simulations, the evolution of system (6) has been initiated either by single Gaussian perturbation of V_z or by a set of analytical eigenfunctions (8)–(15) of zero eigenmode. The discrepancy between these starting functions and the solution of (6) grows with increasing value of k. Nevertheless, in both cases and for all k values, the solution converges to the same purely oscillating (up to numerical damping) mode with identical eigenfrequency $\omega(k)$. This suggests that the flapping oscillations can be triggered by arbitrary initial perturbations bearing some resemblance to the solutions of system (6).

Perturbations similar to a Gaussian perturbation of V_z velocity may be caused by many reasons. In particular, one possible mechanism was considered in Ref. 51, where it was shown that bursty bulk flows (BBFs) may produce kink-type oscillations of the current sheet. This mechanism has a substantial advantage, because it may explain the non-zero x-component of the wave vector of some flapping wave fronts observed in the magnetotail.[10] On the other hand, the DG model represents a long-wavelength limit of the general ballooning mode.[34] Generally speaking, the wave vector of the latter has $k_x \neq 0$, while $\mathbf{k} = (0, k_y, 0)$ is a limiting case only. In view of that, a generalization of the numerical and analytical models for the case of non-zero k_x is the challenging subject for future studies.

ACKNOWLEDGMENTS

Numerical simulations are performed by D.B.K. and S.A.K., supported by the Austrian Science Fund (FWF): P 27012-N27. The work of I.B.I. and V.S.S on the code development was supported by Russian Scientific Fund (RSF) Grant No. 14-17-00072. Analytical approach was elaborated by N.V.E. with the support of RFBR Grant No. 15-05-00879-a. The work of I.B.I. was greatly supported by his wife. Authors thank the reviewer for his help in the manuscript improvement, and Professor V. A. Sergeev and Dr. I. Y. Vasko for fruitful discussions.

APPENDIX: FLUX DENSITIES AND SOURCE FUNCTION

The flux densities $\mathbf{F}_x$ and $\mathbf{F}_z$, and the source function $\mathbf{S}$ of the Eq. (6) are given in the following expressions:

$$F_{x1} = V_{0x}\delta\rho + \rho_0\delta V_x,$$

$$F_{x2} = V_{0x}^2\delta\rho + 2\rho_0 V_{0x}\delta V_x - 2B_{0x}\delta B_x + \delta p + (\mathbf{B}_0 \cdot \delta\mathbf{B}),$$

$$F_{x3} = \rho_0(V_{0x}\delta V_y + V_{0y}\delta V_x) + V_{0x}V_{0y}\delta\rho - B_{0x}\delta B_y - B_{0y}\delta B_x,$$

$$F_{x4} = \rho_0(V_{0x}\delta V_z + V_{0z}\delta V_x) + V_{0x}V_{0z}\delta\rho - B_{0x}\delta B_z - B_{0z}\delta B_x,$$

$$F_{x5} = 0,$$

$$F_{x6} = V_{0x}\delta B_y + B_{0y}\delta V_x - B_{0x}\delta V_y - V_{0y}\delta B_x,$$

$$F_{x7} = V_{0x}\delta B_z + B_{0z}\delta V_x - B_{0x}\delta V_z - V_{0z}\delta B_x,$$

$$F_{x8} = \delta(\hat{E}V_x) - B_{0x}[(\mathbf{B}_0 \cdot \delta\mathbf{V}) + (\mathbf{V}_0 \cdot \delta\mathbf{B})] - (\mathbf{B}_0 \cdot \mathbf{V}_0)\delta B_x,$$

$$F_{z1} = V_{0z}\delta\rho + \rho_0\delta V_z,$$

$$F_{z2} = \rho_0(V_{0x}\delta V_z + V_{0z}\delta V_x) + V_{0x}V_{0z}\delta\rho - B_{0z}\delta B_x - B_{0x}\delta B_z,$$

$$F_{z3} = \rho_0(V_{0y}\delta V_z + V_{0z}\delta V_y) + V_{0y}V_{0z}\delta\rho - B_{0z}\delta B_y - B_{0y}\delta B_z,$$

$$F_{z4} = V_{0z}^2\delta\rho + 2\rho_0 V_{0z}\delta V_z - 2B_{0z}\delta B_z + \delta p + (\mathbf{B}_0 \cdot \delta\mathbf{B}),$$

$$F_{z5} = V_{0z}\delta B_x + B_{0x}\delta V_z - B_{0z}\delta V_x - V_{0x}\delta B_z,$$

$$F_{z6} = V_{0z}\delta B_y + B_{0y}\delta V_z - B_{0z}\delta V_y - V_{0y}\delta B_z,$$

$$F_{z7} = 0,$$

$$F_{z8} = \delta(\hat{E}V_z) - B_{0z}[(\mathbf{B}_0\cdot\delta\mathbf{V}) + (\mathbf{V}_0\cdot\delta\mathbf{B})] - (\mathbf{B}_0\cdot\mathbf{V}_0)\delta B_z,$$

$$S_1 = -ik[V_{0y}\delta\rho + \rho_0\delta V_y],$$

$$S_2 = -ik[\rho_0(V_{0x}\delta V_y + V_{0y}\delta V_x) + V_{0x}V_{0y}\delta\rho - B_{0x}\delta B_y - B_{0y}\delta B_x],$$

$$S_3 = -ik[V_{0y}^2\delta\rho + 2\rho_0 V_{0y}\delta V_y - 2B_{0y}\delta B_y + \delta p + (\mathbf{B}_0\cdot\delta\mathbf{B})],$$

$$S_4 = -ik[\rho_0(V_{0z}\delta V_y + V_{0y}\delta V_z) + V_{0y}V_{0z}\delta\rho - B_{0y}\delta B_z - B_{0z}\delta B_y],$$

$$S_5 = -ik[V_{0y}\delta B_x + B_{0x}\delta V_y - B_{0y}\delta V_x - V_{0x}\delta B_y],$$

$$S_6 = 0,$$

$$S_7 = -ik[V_{0y}\delta B_z + B_{0z}\delta V_y - B_{0y}\delta V_z - V_{0z}\delta B_y],$$

$$S_8 = -ik[\delta(\hat{E}V_y) - B_{0y}[(\mathbf{B}_0\cdot\delta\mathbf{V}) + (\mathbf{V}_0\cdot\delta\mathbf{B})] - (\mathbf{B}_0\cdot\mathbf{V}_0)\delta B_y],$$

where

$$\delta(\hat{E}V_j) = (\hat{E}_0\delta V_j + V_{0j}\delta\hat{E})|_{j=\{x,y,z\}},$$

$$\hat{E}_0 = 0.5\rho_0 V_0^2 + B_0^2 + p_0\kappa/(\kappa-1),$$

$$\delta\hat{E} = \delta E + \delta p + (\mathbf{B}_0\cdot\delta\mathbf{B}),$$

$$\delta p = (\kappa-1)(\delta E - 0.5V_0^2\delta\rho - \rho_0(\mathbf{V}_0\cdot\delta\mathbf{V}) - (\mathbf{B}_0\cdot\delta\mathbf{B})).$$

[1] N. F. Ness, "The Earth's magnetic tail," J. Geophys. Res. **70**, 2989–3005, doi:10.1029/JZ070i013p02989 (1965).

[2] V. Sergeev, V. Angelopoulos, C. Carlson, and P. Sutcliffe, "Current sheet measurements within a flapping plasma sheet," J. Geophys. Res. **103**, 9177–9187, doi:10.1029/97JA02093 (1998).

[3] T. L. Zhang, W. Baumjohann, R. Nakamura, A. Balogh, and K.-H. Glassmeier, "A wavy twisted neutral sheet observed by CLUSTER," Geophys. Res. Lett. **29**, 1899, doi:10.1029/2002GL015544 (2002).

[4] C. Shen, X. Li, M. Dunlop, Z. X. Liu, A. Balogh, D. N. Baker, M. Hapgood, and X. Wang, "Analyses on the geometrical structure of magnetic field in the current sheet based on cluster measurements," J. Geophys. Res. **108**, 1168, doi:10.1029/2002JA009612 (2003).

[5] V. Sergeev, A. Runov, W. Baumjohann, R. Nakamura, T. L. Zhang, M. Volwerk, A. Balogh, H. Rème, J. A. Sauvaud, M. André, and B. Klecker, "Current sheet flapping motion and structure observed by Cluster," Geophys. Res. Lett. **30**, 1327, doi:10.1029/2002GL016500 (2003).

[6] V. Sergeev, A. Runov, W. Baumjohann, R. Nakamura, T. L. Zhang, A. Balogh, P. Louarnd, J.-A. Sauvaud, and H. Rème, "Orientation and propagation of current sheet oscillations," Geophys. Res. Lett. **31**, L05807, doi:10.1029/2003GL019346 (2004).

[7] V. Sergeev, A. Runov, W. Baumjohann, R. Nakamura, T. L. Zhang, S. Apatenkov, A. Balogh, H. Rème, and J. A. Sauvaud, "Cluster results on the magnetotail current sheet structure and dynamics," in *Proceedings of the Cluster and Double Star Symposium–5th Anniversary of Cluster in Space* (ESA Special Publication, 2006), Vol. 598.

[8] A. Runov, V. A. Sergeev, W. Baumjohann, R. Nakamura, S. Apatenkov, Y. Asano, M. Volwerk, Z. Vörös, T. L. Zhang, A. Petrukovich *et al.*, "Electric current and magnetic field geometry in flapping magnetotail current sheets," Ann. Geophys. **23**, 1391–1403 (2005).

[9] A. Runov, V. Sergeev, R. Nakamura, W. Baumjohann, S. Apatenkov, Y. Asano, T. Takada, M. Volwerk, Z. Vörös, T. L. Zhang *et al.*, "Local structure of the magnetotail current sheet: 2001 Cluster observations," Ann. Geophys. **24**, 247–262 (2006).

[10] A. Runov, V. Angelopoulos, V. A. Sergeev, K. H. Glassmeier, U. Auster, J. McFadden, D. Larson, and I. Mann, "Global properties of magnetotail current sheet flapping: THEMIS perspectives," Ann. Geophys. **27**, 319–328 (2009).

[11] A. A. Petrukovich, W. Baumjohann, R. Nakamura, A. Runov, A. Balogh, and C. Carr, "Oscillatory magnetic flux tube slippage in the plasma sheet," Ann. Geophys. **24**, 1695–1704 (2006).

[12] C. Shen, Z. Rong, X. Li, M. Dunlop, Z. Liu, H. Malova, E. Lucek, and C. Carr, "Magnetic configurations of the tilted current sheets in magnetotail," Ann. Geophys. **26**, 3525–3543 (2008).

[13] B. H. Mauk, D. C. Hamilton, T. W. Hill, G. B. Hospodarsky, R. E. Johnson, C. Paranicas, E. Roussos, C. T. Russell, D. E. Shemansky, E. C. Sittler *et al.*, "Fundamental plasma processes in Saturn's magnetosphere," in *Saturn from Cassini-Huygens*, edited by M. K. Dougherty, L. W. Esposito, and S. M. Krimigis (Springer, 2009), pp. 281–331.

[14] Z. Rong, C. Shen, A. Petrukovich, W. Wan, and Z. Liu, "The analytic properties of the flapping current sheets in the earth magnetotail," Planet. Space Sci. **58**, 1215–1229 (2010).

[15] M. Volwerk, N. André, C. S. Arridge, C. M. Jackman, X. Jia, S. E. Milan, A. Radioti, M. F. Vogt, A. P. Walsh, R. Nakamura *et al.*, "Comparative magnetotail flapping: An overview of selected events at Earth, Jupiter and Saturn," Ann. Geophys. **31**, 817–833 (2013).

[16] G. Wang, M. Volwerk, R. Nakamura, P. Boakes, T. Zhang, A. Yoshikawa, and D. Baishev, "Flapping current sheet with superposed waves seen in space and on the ground," J. Geophys. Res. (Space Phys.) **119**, 10078 (2014).

[17] Z. Rong, S. Barabash, G. Stenberg, Y. Futaana, T. Zhang, W. Wan, Y. Wei, X. Wang, L. Chai, and J. Zhong, "The flapping motion of the venusian magnetotail: Venus express observations," J. Geophys. Res. (Space Phys.) **120**, 5593–5602 (2015).

[18] M. Hoshino, A. Nishida, T. Mukai, Y. Saito, T. Yamamoto, and S. Kokubun, "Structure of plasma sheet current in distant magnetotail: Double-peaked electric current sheet," J. Geophys. Res. **101**, 24775–24786, doi:10.1029/96JA02313 (1996).

[19] I. Vasko, A. Petrukovich, A. Artemyev, R. Nakamura, and L. Zelenyi, "Earth's distant magnetotail current sheet near and beyond lunar orbit," J. Geophys. Res. (Space Phys.) **120**, 8663–8680 (2015).

[20] N. V. Erkaev, V. S. Semenov, and H. K. Biernat, "Magnetic double-gradient instability and flapping waves in a current sheet," Phys. Rev. Lett. **99**, 235003 (2007).

[21] N. V. Erkaev, V. S. Semenov, I. V. Kubyshkin, M. V. Kubyshkina, and H. K. Biernat, "MHD aspect of current sheet oscillations related to magnetic field gradients," Ann. Geophys. **27**, 417–425 (2009).

[22] C. Forsyth, M. Lester, R. C. Fear, E. Lucek, I. Dandouras, A. N. Fazakerley, H. Singer, and T. K. Yeoman, "Solar wind and substorm excitation of the wavy current sheet," Ann. Geophys. **27**, 2457–2474 (2009).

[23] W. Sun, S. Fu, Q. Shi, Q. Zong, Z. Yao, T. Xiao, and G. Parks, "THEMIS observation of a magnetotail current sheet flapping wave," Chin. Sci. Bull. **59**, 154–161 (2014).

[24] I. V. Golovchanskaya and Y. P. Maltsev, "On the identification of plasma sheet flapping waves observed by cluster," Geophys. Res. Lett. **32**, L02102, doi:10.1029/2004GL021552 (2005).

[25] I. V. Golovchanskaya, A. Kullen, Y. P. Maltsev, and H. Biernat, "Ballooning instability at the plasma sheet-lobe interface and its implications for polar arc formation," J. Geophys. Res. **111**, 11216, doi:10.1029/2005JA011092 (2006).

[26] N. G. Mazur, E. N. Fedorov, and V. A. Pilipenko, "Dispersion relation for ballooning modes and condition of their stability in the near-Earth plasma," Geomag. Aeron. **52**, 603–612 (2012).

[27] W. Daughton, "Kinetic theory of the drift kink instability in a current sheet," J. Geophys. Res. **103**, 29429–29443, doi:10.1029/1998JA900028 (1998).

[28] W. Daughton, "Two-fluid theory of the drift kink instability," J. Geophys. Res. **104**, 28701–28707, doi:10.1029/1999JA900388 (1999).

[29] H. Karimabadi, W. Daughton, P. L. Pritchett, and D. Krauss-Varban, "Ion-ion kink instability in the magnetotail: 1. linear theory," J. Geophys. Res. **108**, 1400, doi:10.1029/2003JA010026 (2003).

[30] H. Karimabadi, P. L. Pritchett, W. Daughton, and D. Krauss-Varban, "Ion-ion kink instability in the magnetotail: 2. three-dimensional full particle and hybrid simulations and comparison with observations," J. Geophys. Res. **108**, 1401, doi:10.1029/2003JA010109 (2003).

[31] M. I. Sitnov, M. Swisdak, J. F. Drake, P. N. Guzdar, and B. N. Rogers, "A model of the bifurcated current sheet: 2. flapping motions," Geophys. Res. Lett. **31**, L09805, doi:10.1029/2004GL019473 (2004).

[32] P. Ricci, G. Lapenta, and J. U. Brackbill, "Structure of the magnetotail current: Kinetic simulation and comparison with satellite observations," Geophys. Res. Lett. **31**, L06801, doi:10.1029/2003GL019207 (2004).

[33] L. M. Zelenyi, A. V. Artemyev, A. A. Petrukovich, R. Nakamura, H. V. Malova, and V. Y. Popov, "Low frequency eigenmodes of thin anisotropic current sheets and cluster observations," Ann. Geophys. **27**, 861–868 (2009).

[34] D. B. Korovinskiy, A. Divin, N. V. Erkaev, V. V. Ivanova, I. B. Ivanov, V. S. Semenov, G. Lapenta, S. Markidis, H. K. Biernat, and M. Zellinger, "MHD modeling of the double-gradient (kink) magnetic instability," J. Geophys. Res. **118**, 1146–1158, doi:10.1002/jgra.50206 (2013).

[35] D. Korovinskiy, A. Divin, N. Erkaev, V. Semenov, A. Artemyev, V. Ivanova, I. Ivanov, G. Lapenta, S. Markidis, and H. Biernat, "The double-gradient magnetic instability: Stabilizing effect of the guide field," Phys. Plasma **22**, 012904 (2015).

[36] J. D. Huba, J. F. Drake, and N. T. Gladd, "Lower-hybrid-drift instability in field reversed plasmas," Phys. Fluids **23**, 552–561 (1980).

[37] L. N. Hau, R. A. Wolf, G. H. Voigt, and C. C. Wu, "Steady state magnetic field configurations for the Earth's magnetotail," J. Geophys. Res. **94**, 1303–1316, doi:10.1029/JA094iA02p01303 (1989).

[38] A. Miura, S. Ohtani, and T. Tamao, "Ballooning instability and structure of diamagnetic hydromagnetic waves in a model magnetosphere," J. Geophys. Res. **94**, 15231–15242, doi:10.1029/JA094iA11p15231 (1989).

[39] D.-Y. Lee and R. A. Wolf, "Is the Earth's magnetotail balloon unstable?" J. Geophys. Res. **97**, 19251–19257, doi:10.1029/92JA00875 (1992).

[40] W. W. Liu, "Physics of the explosive growth phase: Ballooning instability revisited," J. Geophys. Res. **102**, 4927–4931, doi:10.1029/96JA03561 (1997).

[41] P. L. Pritchett and F. V. Coroniti, "A kinetic ballooning/interchange instability in the magnetotail," J. Geophys. Res. **115**, A06301, doi:10.1029/2009JA014752 (2010).

[42] M. I. Sitnov and K. Schindler, "Tearing stability of a multiscale magnetotail current sheet," Geophys. Res. Lett. **37**, L08102, doi:10.1029/2010GL042961 (2010).

[43] J. Raeder, P. Zhu, Y. Ge, and G. Siscoe, "Open geospace general circulation model simulation of a substorm: Axial tail instability and ballooning mode preceding substorm onset," J. Geophys. Res. **115**, A00I16, doi:10.1029/2010JA015876 (2010).

[44] D. B. Korovinskiy, V. V. Ivanova, N. V. Erkaev, V. S. Semenov, I. B. Ivanov, H. K. Biernat, and M. Zellinger, "Kink-like mode of a double gradient instability in a compressible plasma current sheet," Adv. Space Res. **48**, 1531–1536 (2011).

[45] A. G. Kulikovskii, N. V. Pogorelov, and A. Y. Semenov, *Mathematical Aspects of Numerical Solution of Hyperbolic Systems* (CRC Press, 2000).

[46] A. Kurganov, S. Noelle, and G. Petrova, "Semidiscrete central-upwind schemes for hyperbolic conservation laws and hamilton–jacobi equations," SIAM J. Sci. Comp. **23**, 707–740 (2001).

[47] S. Gottlieb, C.-W. Shu, and E. Tadmor, "Strong stability-preserving high-order time discretization methods," SIAM Rev. **43**, 89–112 (2001).

[48] G. Tóth, "The $\nabla \cdot B = 0$ constraint in shock-capturing magnetohydrodynamics codes," J. Comput. Phys. **161**, 605–652 (2000).

[49] N. Erkaev, V. Semenov, and H. Biernat, "Current sheet oscillations in the magnetic filament approach," Phys. Plasma **19**, 062905 (2012).

[50] N. V. Erkaev, V. S. Semenov, and H. K. Biernat, "Hall magnetohydrodynamic effects for current sheet flapping oscillations related to the magnetic double gradient mechanism," Phys. Plasma **17**, 060703 (2010).

[51] N. V. Erkaev, V. S. Semenov, I. V. Kubyshkin, M. V. Kubyshkina, and H. K. Biernat, "MHD model of the flapping motions in the magnetotail current sheet," J. Geophys. Res. **114**, A03206, doi:10.1029/2008JA013728 (2009).

[52] T. Toichi and T. Miyazaki, "Flapping motions of the tail plasma sheet induced by the interplanetary magnetic field variations," Planet. Space Sci. **24**, 147–159 (1976).

[53] M. H. Saito, L.-N. Hau, C.-C. Hung, Y.-T. Lai, and Y.-C. Chou, "Spatial profile of magnetic field in the near-Earth plasma sheet prior to dipolarization by THEMIS: Feature of minimum B," Geophys. Res. Lett. **37**, L08106, doi:10.1029/2010GL042813 (2010).

[54] D. I. Kubyshkina, D. A. Sormakov, V. A. Sergeev, V. S. Semenov, N. V. Erkaev, I. V. Kubyshkin, N. Y. Ganushkina, and S. V. Dubyagin, "How to distinguish between kink and sausage modes in flapping oscillations?" J. Geophys. Res. **119**, 3002–3015, doi:10.1002/2013JA019477 (2014).

[55] A. A. Petrukovich, A. V. Artemyev, R. Nakamura, E. V. Panov, and W. Baumjohann, "Cluster observations of $\partial Bz/\partial x$ during growth phase magnetotail stretching intervals," J. Geophys. Res. **118**, 5720–5730, doi:10.1002/jgra.50550 (2013).